

Electrochemical performance of molybdenum carbide MXene-few-layer graphene hybrid electrodes for aqueous supercapacitors

Original

Electrochemical performance of molybdenum carbide MXene-few-layer graphene hybrid electrodes for aqueous supercapacitors / Vaez, Samaneh; Bagheri, Ahmad; Beydaghi, Hossein; Bellani, Sebastiano; Prenger, Kaitlyn; Guo, Xuyun; Panda, Jaya-Kumar; Wang, Mengjiao; Morengi, Alberto; Makaryan, Taron; Nia, Ali Shaygan; Nicolosi, Valeria; Gatti, Teresa; Bonaccorso, Francesco. - In: NPJ 2D MATERIALS AND APPLICATIONS. - ISSN 2397-7132. - (2026). [10.1038/s41699-026-00709-x]

Availability:

This version is available at: 11583/3011513 since: 2026-05-28T09:57:00Z

Publisher:

Springer Nature

Published

DOI:10.1038/s41699-026-00709-x

Terms of use:

This article is made available under terms and conditions as specified in the corresponding bibliographic description in the repository

Publisher copyright

(Article begins on next page)

Electrochemical performance of molybdenum carbide MXene-few-layer graphene hybrid electrodes for aqueous supercapacitors

Received: 18 February 2026

Accepted: 12 May 2026

Cite this article as: Vaez, S., Bagheri, A., Beydaghi, H. *et al.* Electrochemical performance of molybdenum carbide MXene-few-layer graphene hybrid electrodes for aqueous supercapacitors. *npj 2D Mater Appl* (2026). <https://doi.org/10.1038/s41699-026-00709-x>

Samaneh Vaez, Ahmad Bagheri, Hossein Beydaghi, Sebastiano Bellani, Kaitlyn Prenger, Xuyun Guo, Jaya-Kumar Panda, Mengjiao Wang, Alberto Morengi, Taron Makaryan, Ali Shaygan Nia, Valeria Nicolosi, Teresa Gatti & Francesco Bonaccorso

We are providing an unedited version of this manuscript to give early access to its findings. Before final publication, the manuscript will undergo further editing. Please note there may be errors present which affect the content, and all legal disclaimers apply.

If this paper is publishing under a Transparent Peer Review model then Peer Review reports will publish with the final article.

Electrochemical Performance of Molybdenum Carbide MXene-Few Layer Graphene Hybrid Electrodes for Aqueous Supercapacitors

Samaneh Vaez,^{a,b} Ahmad Bagheri,^{a,c,d} Hossein Beydaghi,^a Sebastiano Bellani,^{a,e} Kaitlyn Prenger,^f Xuyun Guo,^f Jaya-Kumar Panda,^a Mengjiao Wang,^b Alberto Morenghi,^a Taron Makaryan,^g Ali Shaygan Nia,^{c,d} Valeria Nicolosi,^f Teresa Gatti,^{b,h} and Francesco Bonaccorso^{a}*

^a BeDimensional S.p.A., Lungotorrente Secca 30R, 16163 Genoa, Italy

^b Department of Applied Science and Technology (DISAT), Politecnico di Torino, 10129 Torino, Italy

^c Max Planck Institute of Microstructure Physics, Weinberg 2, 06120 Halle, Germany

^d Center for Advancing Electronics Dresden (cfaed) and Faculty of Chemistry and Food Chemistry, Technische Universität Dresden, 01062 Dresden, Germany

^e Antares Electrolysis S.r.l., Piazza della Vittoria 14/19, 16121 Genova, Italy

^f School of Chemistry Centre for Research on Adaptive Nanostructures and Nanodevices (CRANN) and Advanced Materials Bio-Engineering Research Centre (AMBER) Trinity College Dublin, Dublin D02PN40, Ireland

^g Skeleton Technologies GmbH, Göhrenzer Straße 1, 04420 Markranstädt, Germany

^h Center for Materials Research, Justus Liebig University, Heinrich-Buff-Ring 17, 35392 Giessen, Germany

*Corresponding author: f.bonaccorso@bedimensional.it

Abstract

This work investigates the influence of ionic radius on the charge storage behavior of molybdenum carbide MXene electrodes (Mo_2CCl_2) produced through the molten salt etching method for application in aqueous-based supercapacitors (SCs). Various electrolytes, *i.e.*, 3 M H_2SO_4 , 1 M Li_2SO_4 , 1 M Na_2SO_4 , and 0.6 M K_2SO_4 were investigated, revealing that the small cation (H^+) enhances the SCs capacitance through fast redox kinetics and high ionic mobility. To elucidate the role of anions, neutral electrolytes (8 m NaNO_3 , 2 M NaCl , and 1 M Na_2SO_4) were also explored, enabling a wide voltage window and stable operation of SCs. An asymmetric supercapacitor was assembled using $\text{Mo}_2\text{CCl}_2/\text{FLG}$ (few-layer graphene) as the pseudocapacitive electrode and $\text{FLG}/\text{CG}/$ (curved graphene) as the EDLC counterpart. In this configuration, FLG prevents MXene restacking while CG provides abundant electroactive sites,

resulting in enhanced energy density and cycling durability. These results highlight the combined effect of electrolyte ion selection and hybrid electrode engineering toward high-performance, durable aqueous energy-storage devices.

Keywords

MXenes, Molten Salt Etching, Supercapacitor, Few-layer Graphene, Curved Graphene

Introduction

The demand for energy is increasing worldwide due to population growth and industrial development.^{1,2} At the same time, renewable energy sources are increasingly being used to reduce dependence on fossil fuels.³ Supercapacitors (SCs) are considered promising energy storage devices due to their unique properties, including fast charge-discharge, high specific power, and excellent cyclic stability.^{4,5} Supercapacitors are mainly divided into two types: electrochemical double-layer capacitors (EDLCs)⁶ and pseudocapacitors (PCs).⁶⁻⁸ In EDLCs, energy is stored electrostatically through the adsorption and desorption of ions at the electrode–electrolyte interface.⁹ However, EDLCs are limited by low energy density, which restricts their use in large-scale energy storage applications.¹⁰⁻¹³

In contrast, PCs utilize rapid and reversible faradaic processes, including redox reactions, ion intercalation, and electrosorption, to achieve significantly higher charge storage capacity compared to EDLCs.^{1,14,15} This faradaic contribution enhances the energy density of PCs while maintaining the fast charge–discharge kinetics characteristic of SCs.^{16,17} As a result, PCs are considered as strong candidates for next-generation energy storage systems, although further advances in electrode materials and device design are still needed to overcome unsolved challenges. The latter include sluggish ion transport within dense electrode architectures,^{18,19} structural degradation during repeated redox cycling,^{20,21} and mismatched potential windows between electrodes and electrolytes,^{22,23} all of which adversely affect the long-term cycling stability of PCs. Several two-dimensional (2D) materials, including, manganese dioxide (MnO₂), molybdenum disulfide (MoS₂), tungsten disulfide (WS₂), and MXenes, have emerged as promising candidates for pseudocapacitive energy storage devices.²⁴⁻²⁷ These materials offer high surface area (*i.e.*, ~18–67 m²/g for Ti₃C₂ MXenes), although the reported values vary substantially with processing and architecture.^{28,29} This variability primarily reflects differences in the degree of MXene delamination (which controls interlayer separation and restacking)³⁰ and the formation of composites (*e.g.*, with graphene or other carbonaceous nanomaterials) that inhibit restacking and create more accessible, ion-reachable surface area.^{31,32} Other relevant properties include tunable redox activity³³, and rapid ion-access pathways^{33,34}. However, when used in symmetric PCs, their practical application is often hindered by slow faradaic kinetics (*i.e.*, with charge-transfer resistances R_{ct} ranging from 0.5 to 4 Ω and estimated heterogeneous rate constants k^0 on the order of 10⁻⁹–10⁻⁵ cm/s)³⁵⁻³⁸ and structural instability³⁹, leading to limited rate capability (*i.e.*, capacitance retention drops to 30–60% when current density increases from 1–2 A/g to 10 A/g)^{37,40} and capacity fading over extended cycling (*i.e.*, capacity retention decreases to 70–85% after 3000–5000 cycles).^{16,17,37,40,41.}

To overcome these issues in symmetric PCs, MXenes have recently emerged as promising electrode materials in asymmetric supercapacitors (ASCs) due to their tunable surface chemistry, high electrical conductivity, and intrinsic pseudocapacitive behavior.⁴²⁻⁴⁵ Although other 2D materials can also be used in ASCs, MXenes are highlighted here due to their electrochemical properties. In ASCs, MXenes are often combined with EDLC-type electrodes, enabling simultaneous faradaic and non-faradaic charge storage, which improves energy density while retaining the excellent cycling stability characteristic of EDLCs.^{45,46} In particular, molybdenum carbide MXene (Mo_2CT_x) stands out for its metallic-level electrical conductivity, surface redox chemistry, and layered structure.⁴⁷⁻⁵⁰ These properties enable efficient charge transfer and fast redox kinetics, making Mo_2CT_x particularly suitable for SC applications.^{51,52} Nevertheless, the practical use of Mo_2C is hindered by structural restacking, which occurs during electrode fabrication or repeated cycling. This restacking reduces the ion-accessible surface area (*i.e.*, ~ 8.9 – 4.9 m^2/g)⁵³ and consequently lowers capacitance and rate performance in Mo_2C MXene-based supercapacitors.^{47,54,55}

In this scenario, the integrating chloride-terminated Mo_2C MXene (Mo_2CCl_2) with conductive carbon materials enhances electron transport and mitigates restacking of Mo_2CCl_2 layers, thereby increasing the ion-accessible surface area and improving both rate capability and cycling stability.⁵⁶ In this work, we propose the design and realization of a hybrid electrode composed of Mo_2CCl_2 produced via molten salt etching method⁵⁷ and few-layer graphene (FLG). Although Mo_2CCl_2 exhibits metallic-level conductivity, the actual conductivity strongly depends on surface terminations,⁵⁸ structural defects, flake restacking, and interlayer resistance.^{59,60} In our case, the incorporation of FLG improves the conductive network by reducing interlayer resistance and preventing restacking, thereby enhancing effective charge transport compared to pristine Mo_2CCl_2 .^{55,61-64} The synergistic interaction between Mo_2CCl_2 and FLG enables efficient charge transport, rapid redox kinetics, and enhanced structural stability, leading to improved energy storage performance compared to the pristine counterpart (*i.e.*, the $\text{Mo}_2\text{CCl}_2/\text{FLG}$ electrode delivers 136.3 F/g at 50 mV/s in 3 M H_2SO_4 , compared to ~ 79 F/g reported for Mo_2C -based MXenes).⁵⁴ This hybrid electrode ($\text{Mo}_2\text{CCl}_2/\text{FLG}$) design represents a novel approach for the development of next-generation high-performance SCs. Based on this rationale, the electrochemical behavior of $\text{Mo}_2\text{CCl}_2/\text{FLG}$ electrodes was evaluated in different aqueous electrolytes, beginning with a series of sulfates: 3 M H_2SO_4 , 1 M Li_2SO_4 , 1 M Na_2SO_4 , and 0.6 M K_2SO_4 , to investigate the effect of cation size on electrode performance. Beyond material selection, electrolyte ion characteristics significantly affect charge storage behavior, ionic transport, and overall SC coulombic efficiency (CE).⁶⁵ Aqueous electrolytes, with their inherently high ionic conductivity compared to organic electrolytes and ionic liquids, enable fast charge–discharge operation, offering advantages for high-power applications.^{66,67} Notably, smaller hydrated cations such as H^+ exhibit greater mobility and conductivity than their larger alkali-metal counterparts (Li^+ , Na^+ , K^+), resulting in enhanced capacitive performance in 3 M H_2SO_4 electrolyte.^{65,68} To elucidate the role of anionic radius, 2 M NaCl , 8 m NaNO_3 and 1M Na_2SO_4 electrolytes were used to investigate the influence of anions on charge transport resistance. The electrodes studied are referred to as X–Y, in which X represents the active

material ($\text{Mo}_2\text{CCl}_2/\text{FLG}$) and Y denotes the type of electrolyte used (e.g., H_2SO_4 , NaNO_3 , etc.). Electrochemical characterization was carried out in a three-electrode Swagelok configuration, enabling evaluation of the $\text{Mo}_2\text{CCl}_2/\text{FLG}$ working electrode. A combination of cyclic voltammetry (CV), galvanostatic charge–discharge (GCD), and electrochemical impedance spectroscopy (EIS) was used to comprehensively investigate the charge-storage mechanism, rate capability, and interfacial resistance of the electrodes in various electrolyte systems. The results demonstrated a strong dependence of electrochemical performance on ionic radius. Among the electrolytes investigated, the half-cell based on 3 M H_2SO_4 delivered the highest effective gravimetric capacitance (C_g) of 136.3 F/g at 50 mV/s. This superior performance arises from faster interfacial charge transfer in acidic electrolyte, shown by a lower series resistance ($R_s \approx 0.04 \Omega$ in 3 M H_2SO_4) versus 0.08Ω (2 M NaCl) and 0.13Ω (8 m NaNO_3). Stronger ion adsorption is enabled by the smaller hydrated proton radius (H^+ : 2.76 Å) compared with K^+ (3.31 Å), Na^+ (3.58 Å), and Li^+ (3.82 Å). Enhanced surface redox activity is evidenced by persistent reversible peaks in 3 M H_2SO_4 half-cells across increasing scan rates. The capacitance at 50 mV/s is 136.3 F/g, higher than 42.85 F/g (1 M Li_2SO_4), 38.75 F/g (1 M Na_2SO_4), and 32.12 F/g (0.6 M K_2SO_4), $\sim 3.2\text{--}4.2\times$ higher.

However, to enhance the device-level performance, the pseudocapacitive $\text{Mo}_2\text{CCl}_2/\text{FLG}$ hybrid electrode was assembled with an EDLC electrode offering fast and reversible ion transport capability, forming an asymmetric device. Concerning the EDLC electrode, the composition of curved graphene (CG) with FLG (CG/FLG) was used to prevent nanosheets restacking and enhance the exposure of electroactive surface sites of the CG/FLG electrode, providing excellent structural and electrochemical compatibility with the $\text{Mo}_2\text{CCl}_2/\text{FLG}$ electrode.⁶⁹ The ASCs were assembled and evaluated in three aqueous electrolytes: 3 M H_2SO_4 , 2 M NaCl, and 8 m NaNO_3 , each selected to balance ionic mobility (3 M H_2SO_4), environmental safety, and electrochemical stability (2 M NaCl and 8 m NaNO_3). The as-prepared ASCs are denoted as *negative electrode // positive electrode –electrolyte*, i.e., $\text{Mo}_2\text{CCl}_2/\text{FLG} // \text{CG}/\text{FLG}\text{--}3 \text{ M } \text{H}_2\text{SO}_4$ indicates a device with $\text{Mo}_2\text{CCl}_2/\text{FLG}$ as the negative, CG/FLG as the positive electrode and 3 M H_2SO_4 as the electrolyte. Among the assembled ASCs, the device using 8 m NaNO_3 as the electrolyte delivered the highest electrochemical performance, achieving an energy density of approximately 8 Wh/kg and remarkable cyclic stability (94% gravimetric capacitance $-C_g$ -retention after 12000 GCD cycles). The 2 M NaCl-based ASCs also demonstrated long-term stability (81% C_g retention after 12000 GCD cycles), reaching an energy density of 7.39 Wh/kg, higher than that of the 3 M H_2SO_4 -based ASCs (4 Wh/kg). The 3 M H_2SO_4 -based ASCs delivered the highest C_g but operating at lower cell voltage (1 V), compared with 2 M NaCl- and 8 M NaNO_3 -based ASCs (1.6 V), due to water decomposition under acidic conditions. This study offers significant insights into the electrochemical behavior of the hybrid $\text{Mo}_2\text{CCl}_2/\text{FLG}$ electrode, revealing correlations between its structural properties and potential application in electrochemical energy storage systems.

Results

Figure 1a presents the schematic representation of the Mo_2CCl_2 synthesis. The morphological and structural characterization of the synthesized Mo_2CCl_2 is shown in **Figure 1b-f**. **Figure 1b** shows the X-ray diffraction (XRD) patterns of both the synthesized MXene after copper removal by washing and its parent phase, $\text{Mo}_2\text{Ga}_2\text{C}$. After etching and washing, the XRD pattern changes significantly. Compared with $\text{Mo}_2\text{Ga}_2\text{C}$, the peaks at $\sim 34^\circ$, 37° , and 43° 2θ reduce in intensity by approximately 50–70% and slightly shifted by 0.2° – 0.4° , while the (002) peak at around 9° strongly reduced in intensity. These structural changes are consistent with previously reported molten-salt-synthesized Mo_2CT_x MXenes in literature⁵⁷. The Scanning Electron Microscopy (SEM) image reported in **Figure 1c** reveals several multilayer MXene flakes exhibiting visible slit-like pores. The flakes reach sizes of up to a few micrometers in length and display textured surfaces. **Figure 1d** shows a Selected Area Electron Diffraction (SAED) image of Mo_2CCl_2 along the [001] axis, confirming its hexagonal symmetry and high crystallinity. The High-Angle Annular Dark-Field Scanning Transmission Electron Microscopy (HAADF STEM) image in **Figure 1e**, together with the Transmission Electron Microscopy (TEM) images in **Figure 1f** and **Figure 1j**, further confirm high-quality multilayer MXene flakes. While molten salt etching of MXene^{70,71} differs significantly from conventional aqueous acid etching methods⁷²⁻⁷⁴, the resulting materials retain the characteristic features of MXenes and exhibit excellent structural quality. The $\text{Mo}_2\text{CCl}_2/\text{FLG}$ electrode was evaluated in a three-electrode configuration in various sulfate-based electrolytes (3 M H_2SO_4 , 1 M Li_2SO_4 , 1 M Na_2SO_4 , and 0.6 M K_2SO_4) to investigate the effect of cation radius and mobility on charge storage. The electrolyte concentrations were chosen based on their optimal ionic conductivity, viscosity, and electrochemical stability reported in the literature, rather than identical molar values.⁶⁹ The experimental design enables isolation of cation and anion effects within consistent chemical frameworks.

Figure 2a illustrates the schematic of the three-electrode configuration for the $\text{Mo}_2\text{CCl}_2/\text{FLG}$ electrode tested in various aqueous electrolytes. **Figure 2b** presents the CV curves recorded at a scan rate of 20 mV/s for all electrolytes. The results reveal a predominantly capacitive and irreversible redox behaviour (small oxidation peak) for $\text{Mo}_2\text{CCl}_2/\text{FLG}$ –1 M Li_2SO_4 , $\text{Mo}_2\text{CCl}_2/\text{FLG}$ –1 M Na_2SO_4 , and $\text{Mo}_2\text{CCl}_2/\text{FLG}$ –0.6 M K_2SO_4 . In contrast, $\text{Mo}_2\text{CCl}_2/\text{FLG}$ –3 M H_2SO_4 exhibits a reversible redox process, indicating a distinct electrochemical mechanism under acidic conditions. Among the tested systems, the $\text{Mo}_2\text{CCl}_2/\text{FLG}$ –3 M H_2SO_4 electrode delivers a markedly higher specific current in the CV profiles, indicating a higher C_g compared to the other assembled systems with different electrolytes.⁶⁸ **Figure S1a–d** displays the CV curves of $\text{Mo}_2\text{CCl}_2/\text{FLG}$ –3 M H_2SO_4 , $\text{Mo}_2\text{CCl}_2/\text{FLG}$ –1 M Li_2SO_4 , $\text{Mo}_2\text{CCl}_2/\text{FLG}$ –1 M Na_2SO_4 , and $\text{Mo}_2\text{CCl}_2/\text{FLG}$ –0.6 M K_2SO_4 recorded at various potential scan rates, ranging from 5 to 50 mV/s. These curves exhibit distinct reversible redox peaks, further confirming the pseudocapacitive properties of the $\text{Mo}_2\text{CCl}_2/\text{FLG}$ –3 M H_2SO_4 devices. On the contrary, $\text{Mo}_2\text{CCl}_2/\text{FLG}$ –1 M Li_2SO_4 , $\text{Mo}_2\text{CCl}_2/\text{FLG}$ –1 M Na_2SO_4 , and $\text{Mo}_2\text{CCl}_2/\text{FLG}$ –0.6 M K_2SO_4 ASCs display a predominantly capacitive behavior.

Notably, the redox peaks of the $\text{Mo}_2\text{CCl}_2/\text{FLG}$ –3 M H_2SO_4 remain visible with increasing the potential scan rates, indicating efficient charge transfer (*i.e.*, persistence of oxidation and redox

peaks in the CV profiles across different scan rates) and electrochemical reversibility.⁷⁵ **Figure S2a–d** shows the GCD profiles of Mo₂CCl₂/FLG–3 M H₂SO₄, Mo₂CCl₂/FLG–1 M Li₂SO₄, Mo₂CCl₂/FLG–1 M Na₂SO₄ and Mo₂CCl₂/FLG–0.6 M K₂SO₄ electrodes, respectively, measured at specific currents ranging from 1 to 20 A/g. All electrodes tested in different electrolytes exhibit non-linear voltage–time profiles at various specific currents. The non-linear GCD profile of the Mo₂CCl₂/FLG–3 M H₂SO₄ displays redox features indicative of substantial pseudocapacitive contributions, whereas the GCD curves obtained in the devices based on the other electrolytes exhibit mainly capacitive behavior. **Figure 2c** shows C_g of Mo₂CCl₂/FLG electrode in four different electrolytes as a function of the potential scan rate, calculated from the CV profiles (see Supporting Information, Equation (S1)). Among the investigated systems, the Mo₂CCl₂/FLG–3 M H₂SO₄ demonstrates the highest C_g (e. g., 136.3 F/g at 50 mV/s), outperforming those measured in 1 M Li₂SO₄, 1 M Na₂SO₄, and 0.6 M K₂SO₄ electrolyte systems (42.85, 38.75, and 32.12 F/g for 1 M Li₂SO₄, 1 M Na₂SO₄ and 0.6 M K₂SO₄, respectively, at the same potential scan rate). This enhancement in 3 M H₂SO₄ arises from the high ionic mobility and small hydration sphere radius of H⁺ ions (2.76 Å), which enable a proton hopping between water molecules *via* hydrogen bonding. Compared with K⁺ (3.31 Å), Na⁺ (3.58 Å), and Li⁺ (3.82 Å) ions, H⁺ exhibits the highest molar ionic conductivity.^{65,68} The enhanced conductivity and ionic mobility facilitate rapid charge transfer, while the smaller hydration radius increases ion adsorption at the electrolyte/electrode interface, further promoting faradaic reactions.^{68,76} Consequently, the superior proton dynamics in 3 M H₂SO₄ result in the highest C_g observed (136.3 F/g at 50 mV/s). **Table S1** compares these results with Mo₂C-based electrodes previously reported in literature, highlighting the material strong potential for supercapacitor applications.

The electrochemical stability of Mo₂CCl₂/FLG electrodes was assessed over 12000 GCD cycles at a specific current of 5 A/g. As demonstrated in **Figure S3a–d**, Mo₂CCl₂/FLG–3 M H₂SO₄, Mo₂CCl₂/FLG–1 M Li₂SO₄, Mo₂CCl₂/FLG–1 M Na₂SO₄, and Mo₂CCl₂/FLG–0.6 M K₂SO₄ samples retained 89%, 90%, 93%, and 90% of their initial C_g, respectively. Additionally, all electrodes maintained nearly 100% CE throughout cycling (up to 12000 cycles). These results highlight the long-term stability and electrochemical reversibility of the Mo₂CCl₂/FLG electrodes across these electrolytes. Considering both stability and cost factors, *i.e.*, Na salts are much more abundant and cost-effective than Li salts, Na-based electrolytes are attractive for their use in large-scale and environmentally friendly energy storage devices.^{77,78} To evaluate the effect of anion size on the electrochemical properties, we compared Mo₂CCl₂/FLG electrode in 2 M NaCl, 8 m NaNO₃, and 1 M Na₂SO₄ using a three-electrode cell configuration. The electrolytes have a near-neutral pH (~6–7), contain the same cation (Na⁺) but different anions: Cl⁻, NO₃⁻, and SO₄²⁻ ion. **Figure 2d** displays the non-rectangular shape of CV curves of Mo₂CCl₂/FLG–2 M NaCl, Mo₂CCl₂/FLG–8 m NaNO₃, and Mo₂CCl₂/FLG–1 M Na₂SO₄ systems at 20 mV/s, indicating the pseudocapacitive behavior.⁷⁹ **Figure S4a–b** presents the CV curves of Mo₂CCl₂/FLG in 2 M NaCl and 8 m NaNO₃ electrolytes measured at scan rates from 5 to 50 mV/s. When assembled and tested in three-electrode cell configuration with both 8 m NaNO₃ and 2 M NaCl electrolytes, the electrodes predominantly exhibit capacitive behavior. Whereas a weak redox reaction is

observed in the cell assembled with 2 M NaCl, indicating a minor pseudocapacitive contribution.⁷⁵

Figure S4c–d illustrate the GCD profiles of the Mo₂CCl₂/FLG–2 M NaCl and Mo₂CCl₂/FLG–8 m NaNO₃ system recorded at specific current, ranging from 1 to 20 A/g. All electrodes exhibit approximately linear voltage–time characteristics across the tested specific current range. These results are consistent with the primarily capacitive behavior previously shown by the CV analyses. This behavior arises from interfacial effects rather than significant anion intercalation, driven by differences in ion size, hydration, and specific adsorption.

The C_g of the Mo₂CCl₂/FLG electrode, measured in 2 M NaCl, 8 m NaNO₃, and 1 M Na₂SO₄ electrolytes at various potential scan rates, was calculated from the CV curves shown in **Figure 2e**. C_g increases with decreasing the potential scan rate, reaching 57.5, 51.25, and 42.5 F/g at 5 mV/s for Mo₂CCl₂/FLG–2 M NaCl, Mo₂CCl₂/FLG–8 m NaNO₃ and Mo₂CCl₂/FLG–1 M Na₂SO₄ systems, respectively. This trend is attributed to diffusion limitations and restricted ion transport at the electrode/electrolyte interface at higher scan rate.^{80,81} The SO₄²⁻ ions possess a larger ionic radius compared to NO₃⁻ and Cl⁻ ions.⁸² Moreover, SO₄²⁻ exhibits lower ionic conductivity and mobility compared to Cl⁻ and NO₃⁻.^{83,84} As a result, 1 M Na₂SO₄ aqueous electrolyte delivered poor capacitive performance. As shown in **Figure S5a-b**, the Mo₂CCl₂/FLG electrode demonstrated excellent cycling stability in 2 M NaCl and 8 m NaNO₃, retaining 80% and 82% of its initial C_g, respectively, after 12000 GCD cycles at 5A/g. Additionally, the CE remained close to 100%, confirming the superior electrochemical reversibility of the electrode.

The cyclic stability of representative Mo₂CCl₂/FLG–3 M H₂SO₄ and Mo₂CCl₂/FLG–8 m NaNO₃ systems after 12000 GCD cycles was investigated by post-measurement XRD and Raman spectroscopy. **Figure S6a** displays the XRD patterns of pristine Mo₂CCl₂ and the Mo₂CCl₂/FLG electrodes after long-term cycling stability in 3 M H₂SO₄ and 8 m NaNO₃ electrolytes, enabling a comparison of the structural changes resulting from electrochemical cycling. The electrodes used Mo₂CCl₂/FLG–3 M H₂SO₄ and Mo₂CCl₂/FLG–8 m NaNO₃ systems after 12000 GCD cycles show main diffraction peaks at 34.5°, 38.0°, 39.6°, 52.3°, 61.9°, 69.8°, 75.0°, and 76.0°, corresponding to the (100), (002), (101), (102), (110), (103), (112), and (201) planes of Mo₂C (JCPDS 65-8766).⁸⁵⁻⁸⁸ More in detail, the XRD pattern of the as-prepared pristine Mo₂CCl₂ show sharp, well-defined peaks, indicating a highly crystalline and ordered structure. After the cyclic stability test, some structural changes were observed in the Mo₂CCl₂/FLG. These changes are likely due to repeated ion intercalation and deintercalation, which can cause mechanical stress such as expansion and contraction of Mo₂CCl₂/FLG during the cycling process.^{66,89-91} Additionally, new diffraction peaks appear at 43.5°, 44.9°, and 60° after cycling, indicating the formation of new crystalline phases. These phases may occur from side reactions, the generation of byproducts, or partial decomposition of Mo₂CCl₂.^{92,93} A sharp diffraction peak observed at 54.9° corresponds to the (004) reflection, which is characteristic of graphite (substrate) and FLG, confirming the presence of well-ordered graphitic structures within the electrode.^{62,94}

To further investigate structural changes in Mo₂CCl₂/FLG electrodes after GCD cycling, ex-situ Raman spectroscopy was performed on the electrode of Mo₂CCl₂/FLG–3 M H₂SO₄ and Mo₂CCl₂/FLG–8 m NaNO₃ systems (Figure S6b). Raman spectra reveal characteristic peaks at 1358 cm⁻¹ (D band) and 1583 cm⁻¹ (G band), which are typically observed in graphite, FLG and Mo₂CCl₂.^{85,88,95,96} Additionally, a distinct peak at 886cm⁻¹ is attributed to Mo₂CCl₂.⁹⁵⁻⁹⁷ Notably, these characteristic peaks remain present in the samples after the GCD cycling, indicating that Mo₂CCl₂/FLG electrodes preserved their structural integrity. The Raman I(D)/I(G) ratios for pristine Mo₂CCl₂ and the Mo₂CCl₂/FLG electrode are ~0.77 and ~0.52, respectively, indicating that the incorporation of FLG reduces the overall defect density and improves structural ordering within the composite.⁹⁸ Controlled defect sites are known to enhance the electrochemical performance of carbon-based and MXene electrodes by providing additional electroactive sites and improving ion accessibility, whereas excessive defects can hinder electrical conductivity and limit power performance.^{96,99,100}

After cycling in different electrolytes, the I(D)/I(G) ratios for Mo₂CCl₂/FLG–8 m NaNO₃ and Mo₂CCl₂/FLG–3 M H₂SO₄ increase to ~0.57 and ~0.71, respectively. The increased defects (higher ID/IG) observed in Mo₂CCl₂/FLG–3 M H₂SO₄ sample suggests that the stronger acidic environment induces a higher density of defect sites, which can partially modify the Mo–C bonding environment.¹⁰¹ This findings correlates with the electrochemical results, in which the higher defect density in Mo₂CCl₂/FLG–3 M H₂SO₄ contributes to greater pseudocapacitive activity and higher capacitance.¹⁰²

To further assess the charge storage performance of the MXene-based electrodes in practical applications, aqueous ASCs were assembled using 8 m NaNO₃, 2 M NaCl, and 3 M H₂SO₄ as electrolytes. These were selected based on the high C_g obtained in 3 M H₂SO₄ and the excellent cycling stability demonstrated in the environmentally friendly 8 m NaNO₃ and 2 M NaCl electrolytes. Based on the electrochemical evaluation of Mo₂CCl₂/FLG in a three-electrode setup, Mo₂CCl₂/FLG–3 M H₂SO₄ was selected as the PC electrode, whereas Mo₂CCl₂/FLG–8 m NaNO₃ and Mo₂CCl₂/FLG–2 M NaCl exhibited predominantly capacitive behavior (**Figure S9a-f**). The CG/FLG functioned as an EDLCs electrode, as shown by its electrochemical characterization in 8 m NaNO₃ (**Figure S7a-f**), 2 M NaCl (**Figure S8a-f**). Before ASCs assembly, the active material mass loading of the electrodes was optimized to balance the C_g of the positive and negative electrodes. The working voltage windows (WVW) of the ASCs were determined by combining the stable potential ranges of the separate positive and negative electrodes obtained from separate three-electrode CV measurements carried out at 20 mV/s (**Figure 3a-c**). **Figure 3d-f** shows the electrode potentials vs. Ag/AgCl recorded over time during GCD measurements at a specific current of 1 A/g in the investigated electrolytes. The Mo₂CCl₂/FLG electrode in 8 m NaNO₃ and 2 M NaCl operates in a potential range of –0.7 to +0.2 V, confirming mainly capacitive characteristics, whereas the CG/FLG electrode operated between 0.2 and 0.9 V. Both electrodes remained in the electrochemical stability window during GCD process, thereby effectively avoiding parasitic hydrogen and oxygen evolution reactions (HER and OER). The potential profile of CG/FLG is reproduced over subsequent cycles, confirming the excellent electrochemical stability of this EDLC-type electrodes.

Mo₂CCl₂/FLG provides a minor pseudocapacitive contribution at potentials below 0.0V vs. Ag/AgCl. Mo₂CCl₂/FLG // CG/FLG–3 M H₂SO₄ ASCs stably operate within a WVW of 1.0 V. **Figure 4a** reports the CV curves measured for Mo₂CCl₂/FLG // CG/FLG–8 m NaNO₃, –2 M NaCl, and –3 M H₂SO₄ ASCs, measured at scan rate of 20mV/s, with WVW of 1.6 V, 1.6 V, and 1 V, respectively.

The CV profiles indicate that the charge storage process is primarily ruled by EDLC rather than pseudocapacitive contributions.

Figure 4b presents the GCD profiles measured for Mo₂CCl₂/FLG // CG/FLG–8 m NaNO₃, –2 M NaCl, and –3 M H₂SO₄, at a specific current of 5 A/g. The nearly linear GCD profiles confirm the predominantly capacitive behavior of the ASCs, consistent with the CV analysis. **Figure 4c** shows the C_g calculated from the GCD curves (Supporting Information, Equation (S2)). The Mo₂CCl₂/FLG // CG/FLG–3 M H₂SO₄ ASCs achieved the highest C_g of 29.57 F/g at 1 A/g. The Mo₂CCl₂/FLG // CG/FLG–2 M NaCl and Mo₂CCl₂/FLG // CG/FLG–8 m NaNO₃ ASCs displayed C_g values of 24.67 F/g and 23.13 F/g at 1 A/g, respectively. The superior performance of the Mo₂CCl₂/FLG // CG/FLG–3 M H₂SO₄ compared to Mo₂CCl₂/FLG // CG/FLG–2 M NaCl and Mo₂CCl₂ /FLG // CG/FLG–8 m NaNO₃, is consistent with the results obtained from the three-electrode cell configuration for the negative electrodes, with the contribution of FLG further improving electrical conductivity and mitigating restacking, thereby enabling more efficient charge transport within the device.^{68,103} For all ASCs, the C_g decreased with increasing the specific current, although the devices demonstrated remarkable rate capabilities (e.g., at 20 A/g, the C_g retention was 86%, 65%, and 63% for Mo₂CCl₂/FLG // CG/FLG–3 M H₂SO₄, Mo₂CCl₂/FLG // CG/FLG–2 M NaCl, and Mo₂CCl₂/FLG // CG/FLG–8 m NaNO₃, respectively). As demonstrated in **Figure 4c**, CE of the ASCs exceeds 90% at high specific currents for both Mo₂CCl₂/FLG // CG/FLG–2 M NaCl and Mo₂CCl₂/FLG // CG/FLG–8 m NaNO₃, indicating excellent reversibility of the redox processes. In contrast, the Mo₂CCl₂/FLG // CG/FLG–3 M H₂SO₄ ASCs exhibit a slight reduction in CE at lower specific currents (<5 A/g), which is probably attributed to parasitic reactions commonly encountered in ASCs based on acidic electrolyte, which easily promote HER.²³

The impedance of the electrode–electrolyte interfaces was analyzed through EIS measurements. The complex impedance (Z) of the systems was characterized by analysing the Nyquist plots (–Im[Z] vs. Re[Z]), offering valuable information on charge-transfer and diffusion processes.¹⁰⁴ A Nyquist plot of an SC typically exhibits three distinct regions corresponding to different electrochemical processes: redox reactions appearing in the high-to-mid frequency range, ion diffusion processes dominating the mid-frequency region, and capacitive behavior prevailing at low frequencies.^{6,105} In the high-frequency region, the plot reflects the electrical conductivity of the electrode and the charge-transfer reactions occurring at solid/solid interface.¹⁰⁶⁻¹⁰⁹ Thus, the diameter of the semicircle observed in this region is related to the interfacial resistance between the current collector and the electrode.¹¹⁰⁻¹¹² Instead, the x-axis (Z_{re}) intercept at the highest frequency corresponds to the equivalent series resistance (R_s), which arises from the ionic resistance of the electrolyte and the intrinsic electronic resistance of

the electrodes, distinct from the ion-diffusion processes observed in the mid-frequency region.^{77,104,113} **Figure S10** shows the Nyquist plots for Mo₂CCl₂/FLG // CG/FLG–8 m NaNO₃, Mo₂CCl₂/FLG // CG/FLG–2 M NaCl, and Mo₂CCl₂/FLG // CG/FLG–3 M H₂SO₄. The measurements were recorded over a frequency range of 100 kHz to 10 mHz at open-circuit potential with an AC amplitude of 10 mV. From the analysis of the Nyquist plots, calculated R_s were 0.04, 0.13 and 0.08 Ω for Mo₂CCl₂/FLG // CG/FLG–3 M H₂SO₄, Mo₂CCl₂/FLG // CG/FLG–8 m NaNO₃ and Mo₂CCl₂/FLG // CG/FLG–2 M NaCl, respectively. These values indicate significantly lower resistance and higher ionic conductivity in the acidic electrolytes compared to the near-neutral ones. While the above analysis reflects the overall device behavior, a more detailed understanding of ion transport requires a direct assessment of ionic diffusion. Therefore, EIS measurements (**Figure S11a, S11b**) were further conducted in half-cell configurations to investigate the ionic diffusion characteristics of each electrolyte. The diffusion coefficients of ionic charge carriers were estimated using two complementary approaches based on the electrolyte characteristics. For the acidic electrolyte, which Faradaic contributions are more pronounced, the diffusion coefficient (Equation 1) was derived from the Warburg impedance by fitting the linear region of Z' versus ω^{-1/2} (**Figure S11c**) and extracting the Warburg coefficient (σ) (Equation 2).¹¹⁴

$$D = \frac{0.5R^2T^2}{A^2n^4F^4C^2\sigma^2} \quad (1)$$

$$Z_{real} = R_s + R_{ct} + \sigma \omega^{-1/2} \quad (2)$$

In this approach, D is calculated as a function of the universal gas constant (R), temperature (T), electrode area (A), effective number of electrons transferred (n), Faraday constant (F), ionic concentration (C). In contrast, for the near-neutral electrolytes, the impedance response is dominated by capacitive behavior. Therefore, the diffusion coefficients were estimated using the low frequency resistance–capacitance (R_LC_L) approach (Equation 3).¹¹⁵

$$R_L C_L = t^2 / 3D \quad (3)$$

In which R_L and C_L correspond to the resistance and capacitance in the low-frequency region, respectively. The calculated diffusion coefficients are summarized in **Table S2**, while t is the thickness of the Mo₂CCl₂/FLG electrode. As summarized in **Table S2**, the estimated diffusion coefficients span the range of ~10⁻⁷–10⁻⁶ cm²/s across all investigated electrolytes. Notably, the 3 M H₂SO₄ electrolyte exhibits a comparatively lower apparent diffusion coefficient (~7.0 × 10⁻⁷ cm²/s), while the near neutral electrolytes display higher values on the order of ~10⁻⁶ cm²/s. This behavior indicates that ion transport occurs under confined conditions and is strongly influenced by ion-specific properties, including ionic size, hydration structure, and electrolyte composition.^{116,117}

The pseudocapacitive energy storage of the Mo₂C active material is based on redox reactions involving charge transfer. This behavior occurs along with surface-controlled processes that contribute to EDLC.¹¹⁸ The main type of charge storage can be identified by analyzing CV curves at different scan rates. As previously shown, the CV curves of Mo₂CCl₂/FLG // CG/FLG–8 m

NaNO₃, Mo₂CCl₂/FLG // CG/FLG–2 M NaCl, and Mo₂CCl₂/FLG // CG/FLG–3 M H₂SO₄ were measured at different voltage scan rates from 5 to 1000 mV/s. These data were evaluated using the power law given in Equation 4.

$$i = av^b \quad (4)$$

In which i represents the measured current (A), v is the voltage scan rate (mV/s), and a and b are constants that reflect the contributions of capacitive and faradaic processes. Specifically, for diffusion-controlled behavior, the current is proportional to the square root of the scan rate ($b = 0.5$).⁷⁹ In contrast, for capacitive processes, the current is directly proportional to the scan rate ($b = 1$).⁷⁹ The b -value analysis in this study was performed at the full-cell level rather than on individual electrodes. While this approach is more commonly applied to single-electrode systems to distinguish between capacitive and diffusion-controlled processes, in the present case it provides insight into the overall kinetic behavior of the ASCs. The extracted b -values therefore reflect the combined electrochemical response of the pseudocapacitive Mo₂CCl₂/FLG electrode and the EDLC-type CG/FLG electrode, representing the integrated contribution of both components to the overall charge storage mechanism. **Figures S12a,13a,14a** display the b -values for the Mo₂CCl₂/FLG // CG/FLG–8 m NaNO₃, Mo₂CCl₂/FLG // CG/FLG–2 M NaCl, and Mo₂CCl₂/FLG // CG/FLG –3 M H₂SO₄ as a function of their voltage. Notably, b -values for Mo₂CCl₂/FLG // CG/FLG–8 m NaNO₃, range from 0.72 to 0.93 (**Figure S12a**), indicating that the charge storage involves a combination of both capacitive and diffusion-controlled processes. Similarly, the Mo₂CCl₂/FLG // CG/FLG–2 M NaCl and Mo₂CCl₂/FLG // CG/FLG–3 M H₂SO₄ show b values ranging from 0.5 to 1, indicating a mixed charge storage mechanism involving both capacitive and diffusion-controlled contributions, as expressed by the following equation:⁶

$$i(V) = k_1v + k_2v^{1/2} \quad (5)$$

in which v represents the voltage scan rate (mV/s), k_1v corresponds to the current from surface capacitive contributions, and $k_2v^{1/2}$ accounts for the current arising from diffusion-controlled faradaic processes. Equation (6) can also be written in a different form as:

$$\frac{i(V)}{v^{1/2}} = k_1v + k_2 \quad (6)$$

Accordingly, the values of k_1 and k_2 were obtained from the linear fitting of $i(V)/v^{1/2}$ vs. $v^{1/2}$ (Figures S11b,12b,13b). As shown in **Figures S12c-d,13c-d,14c-d**, the diffusion-controlled charge contributions at a voltage scan rate of 5 mV/s were calculated 64% for Mo₂CCl₂ /FLG // CG/FLG–8 m NaNO₃, 40% for Mo₂CCl₂/FLG // CG/FLG–2 M NaCl, and 49% for Mo₂CCl₂/FLG // CG/FLG–3 M H₂SO₄. **Figures S12c,13c,14c** confirm that capacitive charge storage increases with broadening WWV, while diffusion-controlled faradaic processes are progressively decreased with increasing WWV due to the limited kinetics of faradaic reactions.

Figure 4d displays the Ragone plots (energy density, E_s , vs. power density, P_s) for the investigated ASCs. The Ragone plots were derived from the GCD analysis, as detailed in the Supporting Information (Equations S3 and S4). Despite its highest C_g Mo₂CCl₂/FLG // CG/FLG–3 M H₂SO₄ has shown the lowest energy density among the investigated devices, *i.e.*,

4.07 Wh/kg at 338.54 W/kg. The poor energy density of the ASCs based on H₂SO₄ as the electrolyte is primarily due to the limited WWV.⁶⁵ Interestingly, for the 3 M H₂SO₄ electrolyte, an apparent increase in energy density with increasing power density is observed. This behavior is attributed to a decrease in Faradaic efficiency at low power densities due to irreversible parasitic reactions.⁶⁵ The cyclic stability of Mo₂CCl₂/FLG // CG/FLG ASCs was assessed over 12000 GCD cycles at a specific current of 5 A/g. As illustrated in **Figure 4e**, the Mo₂CCl₂ /FLG // CG/FLG–8 m NaNO₃ and Mo₂CCl₂ /FLG // CG/FLG–2 M NaCl retained 94% and 81% of their initial C_g, respectively. In contrast, Mo₂CCl₂ /FLG // CG/FLG–3 M H₂SO₄ has shown a significant performance reduction, retaining only 20% of its initial C_g after 12000 GCD cycles. The CE remained nearly 100% for the 8 m NaNO₃-based and 2 M NaCl ASCs, while it dropped to 83.74% when using 3 M H₂SO₄ electrolyte.

Discussion

This study highlights the successful integration of Mo₂CCl₂/FLG as a high-performance negative electrode and CG/FLG as a complementary positive electrode in aqueous ASCs. The Mo₂CCl₂/FLG hybrid leverages the synergistic combination of pseudocapacitive Mo₂CCl₂ and highly conductive FLG, leading to enhanced charge-transfer kinetics, superior reversibility, and excellent electrochemical performance.

By systematically investigating different aqueous electrolytes, 3 M H₂SO₄, 2 M NaCl, and 8 m NaNO₃, the study elucidates the role of ionic species in modulating charge storage behavior and interfacial resistance. The ASCs with 3 M H₂SO₄ delivered the highest specific capacitance (29.57 F/g at 1 A/g), attributed to the fast proton mobility and efficient surface redox reactions of Mo₂CCl₂. However, in 3 M H₂SO₄ the device voltage had to be limited to 1.0 V due to acid-promoted water splitting/HER, whereas near-neutral Na-based electrolytes (2 M NaCl, 8 m NaNO₃) enabled a broader 1.6 V window. Moreover, Na-based ASCs have shown superior cycling stability, retaining 94% (8 m NaNO₃) and 81% (2 M NaCl) of the initial capacitance after 12000 cycles, compared with only 20% retention in 3 M H₂SO₄-based ASCs.

Remarkably, the 8 m NaNO₃ ASC achieved an energy density of ~8 Wh/kg with 94% capacitance retention after 12000 GCD cycles, demonstrating outstanding long-term durability. Similarly, the 2 M NaCl ASCs exhibited excellent energy retention and cycling stability. The EIS further revealed a strong electrolyte dependence of the internal resistance, with the lowest R_s (~0.04 Ω) observed in 3 M H₂SO₄-based ASC, while 8 m NaNO₃-one displayed a higher R_s due to reduced ion mobility.

Overall, the Mo₂CCl₂/FLG // CG/FLG architecture, when paired with optimized electrolytes, is demonstrating promising for high-performance, durable, and scalable aqueous supercapacitors. These findings establish valuable design guidelines to tailor electrode–electrolyte interfaces and pave the way toward next-generation electrochemical energy storage systems that balance high energy density, power capability, and long-term stability.

Methods

Materials Synthesis:

Mo₂Ga₂C was supplied by Carbon Ukraine. Sodium chloride (NaCl, 99.5%), potassium chloride (KCl, 99.5%), and hydrochloric acid (HCl, 37%) were obtained from Sigma Aldrich. Copper (II) chloride anhydrous (CuCl₂, 98%), was purchased from Alfa Aesar. To perform the molten salt etching of gallium from Mo₂Ga₂C, a procedure similar to the one in Ref ¹¹⁹ was followed. The ratio was adjusted to account for the extra stoichiometry of gallium. Powders of Mo₂Ga₂C, NaCl, KCl, and CuCl₂ were combined in a 1:6:6:6 ratio and ground with a mortar and pestle for 10 min to ensure uniform particle size and to mix the MAX phase and salts together. The mixed powders were then added to an alumina crucible, covered with a lid, and then the crucible was placed in a glove box transfer chamber and evacuated three times, refilling with Argon, to displace extra oxygen trapped within the powders. The crucible was then promptly placed in a tube furnace with argon flowing at 450 sccm. The tube was allowed to purge for 1 h, and then heated at a rate of 5 °C/min up to 700 °C. It was held at 700 °C for 4 h and then allowed to cool to room temperature, all under flowing argon. After cooling, deionized (DI) water was used to dissolve leftover chloride salts and transfer the materials to a 50 mL centrifuge tube. Extra DI water was used to fill the tube as needed. This was centrifuged for 10 min at 5000 rpm, after which the supernatant was discarded. Three additional cycles of adding 50 mL DI water, resuspending the solid material with vortex mixing, centrifuging, and discarding the supernatant were performed to ensure all leftover chloride salts were dissolved and removed from the product.

To remove copper deposited on the multilayer MXene particles during the molten salt synthesis, the wet powders were added to a solution of 1M CuCl₂ in 2M HCl, with 4x the mass of the CuCl₂ used in the molten salt mixture. This mixture was stirred for 4 h, after which the mixture was decanted into 50 mL centrifuge tubes and washed with excess DI water by centrifuging for 5 min at 5000 rpm, discarding the supernatant, and refilling with DI water and resuspending using vortex mixing until the pH of the supernatant reached ~6. The resulting powders were dried using vacuum filtration followed by vacuum annealing at 200 °C for 2 h to remove bulk water. Samples were stored in a vacuum desiccator until needed.

Characterization

XRD patterns were produced using a Bruker D8 ADVANCE powder diffractometer using Cu K_{α1} (λ=0.154 nm) radiation. Patterns were collected between 3° and 80 2θ with a step size of 0.02° and a dwell time of 1.5 s. SEM was performed on a Zeiss Ultra Plus field-emission SEM electron microscope with an accelerating voltage of 3 keV. Both TEM and STEM images were produced using an uncorrected FEI Titan with Schottky field emission S-FEG source operated at 300 kV.

Electrode Preparation:

The hybrid Mo₂CCl₂/FLG electrode was prepared by mixing Mo₂CCl₂ powder and FLG, exfoliated from graphite by BeDimensional S.p.A. using its proprietary wet-jet milling method,^{94,120-123} with a carboxymethyl cellulose:Styrene-Butadiene Rubber (CMC:SBR) binder (weight ratio 90:5:5). A homogenized slurry was obtained by dispersing Mo₂CCl₂ powder in deionized water by ultrasonic bath, and then FLG, CMC:SBR were added in to the composition

and using a planetary centrifugal mixer.^{124,125} The as prepared slurry was deposited onto a graphite sheet by doctor blade method, which allowed for controlled thickness and even distribution.^{7,10} The electrodes were dried at 60 °C in an oven to completely remove residual moisture and solvents. After drying, the electrodes were precisely punched into discs with a diameter of 8 m. The prepared electrodes exhibited an average active material mass loading of approximately 3 mg/cm².¹²⁶

Three-Electrode Cell Configuration:

Electrochemical characterization was carried out in three-electrode Swagelok cells based on 316L stainless steel or titanium pistons, an insulating PTFE-coated 316L stainless steel body, and PTFE sealing rings. Each cell was assembled with a Mo₂CCl₂/FLG working electrode, an Ag/AgCl reference electrode, high-mass loading activated carbon as counter electrode, and a glass fiber (Whatman GF/A) as the separator. The cell components were tightened in the Swagelok cell to maintain good contact and prevent leakage. All measurements were performed at room temperature (~25 °C). Various aqueous electrolytes were used to investigate the effect of ionic radius of different cations and anions on SC performance. These included 3 M H₂SO₄, 1 M Li₂SO₄, 1 M Na₂SO₄, 0.6 M K₂SO₄ (sulfate-based electrolytes for cation comparison), as well as 2 M NaCl and 8 m NaNO₃ (for anion comparison).

ASC Assembly:

Two-electrode ASCs were assembled using Mo₂CCl₂/FLG as the negative electrode and CG/FLG as the positive electrode. The CG/FLG positive electrode was prepared by mixing CG, FLG, and CMC:SBR in water by a planetary centrifugal mixer (weight ratio 90:5:5), and casting the resulting slurry onto a graphite sheet. Before assembling the ASCs, the electrochemical properties of both Mo₂CCl₂/FLG and CG/FLG electrodes were individually evaluated through three-electrode cell measurements. Charge balance between the two electrodes was achieved by adjusting their mass loadings according to their respective charge storage capacities within the selected potential window.^{106,127-129} The optimal mass ratio between the positive and negative electrodes (m_+/m_-) is determined using the following equation 7:

$$\frac{m_+}{m_-} = \frac{C_- \times \Delta V_-}{C_+ \times \Delta V_+} \quad (7)$$

The Mo₂CCl₂/FLG // CG/FLG ASCs were tested in three different aqueous electrolytes: 3 M H₂SO₄, 2 M NaCl, and 8 m NaNO₃. For the 3 M H₂SO₄ electrolyte, the cell voltage was limited to 1.0 V to avoid parasitic water splitting reaction, in particular the acid-promoted HER.^{130,131} In near-neutral 2 M NaCl and 8 m NaNO₃ electrolytes, an upper cell voltage of 1.6 V was reached, taking advantage of the larger overpotential for gas evolution in near-neutral electrolyte.²³ The assembled ASCs were evaluated through CV and GCD analyses. Long-term cyclic stability was assessed by repeating GCD cycles up to 12000 times at a fixed specific current (5 A/g).

Data availability

The datasets generated and/or analyzed during the current study are not publicly available due to confidentiality but are available from the corresponding author on reasonable request.

Acknowledgments

This project received funding from the European Union's 2D Printable Horizon Europe research and innovation program under Grant Agreement No. 101135196 and the European Union's GREENCAP Horizon Europe research and innovation program under Grant Agreement No. 101091572. S.V. acknowledges financial support from the European Union Next Generation EU program (D.M. 117 del 02/03/2023 Ministero dell' Università e della Ricerca). T.G. thanks the European Research Council for the project JANUS BI (grant agreement no. [101041229]) and the European Innovation Council for the project LEAF (grant agreement n. [101186701]). V.N. and X.G. thank the support of the Research Ireland-funded AMBER Research Centre and the SFI Frontiers for the Future award (Grant Nos. 12/RC/2278_P2 and 20/FFP-A/8950 respectively). Furthermore, V.N. and X.G. thank the Advanced Microscopy Laboratory (AML) in CRANN for the provision of their facilities and thank Clive Downing for optimizing the microscope.

Author contributions

S.V.: Collected data, performed the electrochemical analysis, and original draft preparation. A.B. and H.B.: Conceptualization, performed the electrochemical analysis, Supervision, Reviewing & Editing. K.P., X.G., A.S.N., and V.N.: synthesized and characterized the MXenes material. A. M. and T. M. synthesized and characterized the graphene-based material. J-K.P.: performed and analyzed the Raman data and M.W. performed the XRD data. S.B., T.G., and F.B.: Supervision, Reviewing & Editing.

Competing interests

Samaneh Vaez, Ahmad Bagheri, Hossein Beydaghi, Jaya Kumar Panda, Alberto Morenghi and Francesco Bonaccorso are employees of BeDimensional S.p.A., a company producing and commercializing 2D materials. Valeria Nicolosi and Teresa Gatti are Associated Editor of npj 2D Materials and Applications and they were not involved in the journal's review of, or decisions related to, this manuscript. All the other authors declare no conflict of interest.

References

- 1 Qiu, L. *et al.* NiS nanoflake-coated carbon nanofiber electrodes for supercapacitors. *ACS Applied Nano Materials* **5**, 6192-6200 (2022).
- 2 Bagheri, A. *et al.* The effect of adding sulfonated SiO₂ nanoparticles and polymer blending on properties and performance of sulfonated poly ether sulfone membrane: fabrication and optimization. *Electrochimica Acta* **295**, 875-890 (2019).

- 3 Rahman, M. M., Sultana, N. & Velayutham, E. Renewable energy, energy intensity and carbon reduction: Experience of large emerging economies. *Renewable Energy* **184**, 252-265 (2022).
- 4 Garakani, M. A. *et al.* Scalable spray-coated graphene-based electrodes for high-power electrochemical double-layer capacitors operating over a wide range of temperature. *Energy Storage Materials* **34**, 1-11 (2021).
- 5 Chaichi, A., Venugopalan, G., Devireddy, R., Arges, C. & Gartia, M. R. A solid-state and flexible supercapacitor that operates across a wide temperature range. *ACS Applied Energy Materials* **3**, 5693-5704 (2020).
- 6 Noori, A., El-Kady, M. F., Rahmanifar, M. S., Kaner, R. B. & Mousavi, M. F. Towards establishing standard performance metrics for batteries, supercapacitors and beyond. *Chemical Society Reviews* **48**, 1272-1341 (2019).
- 7 Najafi, M. *et al.* Carbon- α -Fe₂O₃ composite active material for high-capacity electrodes with high mass loading and flat current collector for quasi-symmetric supercapacitors. *Electrochem* **3**, 463-478 (2022).
- 8 Iqbal, M. Z. *et al.* Evaluation of d-block metal sulfides as electrode materials for battery-supercapacitor energy storage devices. *Journal of Energy Storage* **55**, 105418 (2022).
- 9 Wang, G., Zhang, L. & Zhang, J. A review of electrode materials for electrochemical supercapacitors. *Chemical Society Reviews* **41**, 797-828 (2012).
- 10 Gamberini, A. *et al.* Ionogel-Based Electrodes for Non-Flammable High-Temperature Operating Electrochemical Double-Layer Capacitors. *ChemSusChem* **18**, e202401874 (2025).
- 11 Gan, Z., Yin, J., Xu, X., Cheng, Y. & Yu, T. Nanostructure and advanced energy storage: elaborate material designs lead to high-rate pseudocapacitive ion storage. *ACS nano* **16**, 5131-5152 (2022).
- 12 Yang, X., Lv, T. & Qiu, J. High mass-loading biomass-based porous carbon electrodes for supercapacitors: review and perspectives. *Small* **19**, 2300336 (2023).
- 13 Pomerantseva, E., Bonaccorso, F., Feng, X., Cui, Y. & Gogotsi, Y. Energy storage: The future enabled by nanomaterials. *Science* **366**, eaan8285 (2019).
- 14 Cong, C. & Ma, H. Advances of electroactive metal-organic frameworks. *Small* **19**, 2207547 (2023).
- 15 Gentile, M. *et al.* Hydrogen-assisted thermal treatment of electrode materials for electrochemical double-layer capacitors. *ACS Applied Materials & Interfaces* **16**, 13706-13718 (2024).
- 16 Lukatskaya, M. R. *et al.* Understanding the mechanism of high capacitance in nickel hexaaminobenzene-based conductive metal-organic frameworks in aqueous electrolytes. *ACS nano* **14**, 15919-15925 (2020).
- 17 Wu, G., Wu, X., Zhu, X., Xu, J. & Bao, N. Two-dimensional hybrid nanosheet-based supercapacitors: from building block architecture, fiber assembly, and fabric construction to wearable applications. *ACS nano* **16**, 10130-10155 (2022).
- 18 Zhu, P., Slater, P. R. & Kendrick, E. Insights into architecture, design and manufacture of electrodes for lithium-ion batteries. *Materials & Design* **223**, 111208 (2022).
- 19 Kress, T., Liu, X. & Forse, A. C. Pore network tortuosity controls fast charging in supercapacitors. *Nature Materials*, 1-7 (2025).
- 20 Chen, X. *et al.* Experimental study on the degradation mechanism of LaCoO₃-based symmetric supercapacitors. *RSC advances* **11**, 25170-25178 (2021).
- 21 Sampaio, R. S., Correia, J. P., Silva, T. & Montemor, M. New insights into the degradation of pseudocapacitive MnOx under floating. *Journal of Energy Storage* **131**, 117546 (2025).

- 22 Forouzandeh, P., Kumaravel, V. & Pillai, S. C. Electrode materials for supercapacitors: a review of recent advances. *Catalysts* **10**, 969 (2020).
- 23 Pameté, E. *et al.* The many deaths of supercapacitors: degradation, aging, and performance fading. *Advanced Energy Materials* **13**, 2301008 (2023).
- 24 Hu, M. *et al.* Emerging 2D MXenes for supercapacitors: status, challenges and prospects. *Chemical Society Reviews* **49**, 6666-6693 (2020).
- 25 Xia, H., Meng, Y. S., Yuan, G., Cui, C. & Lu, L. A symmetric RuO₂/RuO₂ supercapacitor operating at 1.6 V by using a neutral aqueous electrolyte. *Electrochemical and Solid-State Letters* **15**, A60 (2012).
- 26 Ding, J., Hu, W., Paek, E. & Mitlin, D. Review of hybrid ion capacitors: from aqueous to lithium to sodium. *Chemical reviews* **118**, 6457-6498 (2018).
- 27 Crisci, M. *et al.* Easy Direct Functionalization of 2D MoS₂ Applied in Covalent Hybrids with PANI as Dual Blend Supercapacitive Materials. *Advanced Materials Interfaces* **12**, 2400621 (2025).
- 28 Rozmysłowska-Wojciechowska, A. *et al.* Engineering of 2D Ti₃C₂ MXene surface charge and its influence on biological properties. *Materials* **13**, 2347 (2020).
- 29 Borah, A. J., Natu, V., Biswas, A. & Srivastava, A. A review on recent progress in synthesis, properties, and applications of MXenes. *Oxford Open Materials Science* **5**, itae017 (2025).
- 30 Gogotsi, Y. & Anasori, B. in *MXenes* 3-11 (Jenny Stanford Publishing, 2023).
- 31 Zhou, Y. *et al.* Ti₃C₂T_x MXene-reduced graphene oxide composite electrodes for stretchable supercapacitors. *ACS nano* **14**, 3576-3586 (2020).
- 32 Nan, J. *et al.* Nanoengineering of 2D MXene-based materials for energy storage applications. *Small* **17**, 1902085 (2021).
- 33 Nasrin, K., Sudharshan, V., Subramani, K. & Sathish, M. Insights into 2D/2D MXene heterostructures for improved synergy in structure toward next-generation supercapacitors: a review. *Advanced Functional Materials* **32**, 2110267 (2022).
- 34 Shinde, N. M. & Pumera, M. MXene-Based Nanocomposites for Supercapacitors: Fundamentals and Applications. *Small Methods*, 2401751 (2025).
- 35 Bai, P. & Bazant, M. Z. Charge transfer kinetics at the solid–solid interface in porous electrodes. *Nature communications* **5**, 3585 (2014).
- 36 Guo, Y. *et al.* Synthesis of Mo₂C MXene with high electrochemical performance by alkali hydrothermal etching. *J. Adv. Ceram* **12**, 1889-1901 (2023).
- 37 Xu, H. *et al.* High-Temperature Oxidized Mo₂C_{T_x} MXene for a High-Performance Supercapacitor. *ACS Applied Materials & Interfaces* **15**, 53549-53557 (2023).
- 38 Anjum, N. *et al.* Electrochemical Impedance Analysis of Ti₃C₂T_x MXene for Pseudocapacitive Charge Storage. *Journal of Composites Science* **9**, 139 (2025).
- 39 Palisaitis, J., Persson, I., Halim, J., Rosen, J. & Persson, P. O. On the structural stability of MXene and the role of transition metal adatoms. *Nanoscale* **10**, 10850-10855 (2018).
- 40 Liu, H., Chang, X., Li, L. & Zhang, M. Size Engineering of Ti₃C₂T_x Nanosheets for Enhanced Supercapacitive Performance. *Molecules* **30**, 241 (2025).
- 41 Islam, M. S., Mubarak, M. & Lee, H.-J. Hybrid nanostructured materials as electrodes in energy storage devices. *Inorganics* **11**, 183 (2023).
- 42 Panda, S. *et al.* MXene based emerging materials for supercapacitor applications: Recent advances, challenges, and future perspectives. *Coordination Chemistry Reviews* **462**, 214518 (2022).

- 43 Ren, D. *et al.* Development and evaluation of Zn²⁺ ions hybrid supercapacitor based on Zn_xMnO₂-CNTs cathode. *Applied Energy* **324**, 119730 (2022).
- 44 Murali, G. *et al.* A review on MXenes: new-generation 2D materials for supercapacitors. *Sustainable Energy & Fuels* **5**, 5672-5693 (2021).
- 45 Devi, R. K. *et al.* A facile strategy for the synthesis of manganese-doped nickel sulfide nanosheets and oxygen, nitrogen-enriched 3D-graphene-like porous carbon for hybrid supercapacitor. *Journal of Alloys and Compounds* **944**, 169261 (2023).
- 46 Otgonbayar, Z., Yang, S., Kim, I.-J. & Oh, W.-C. Recent advances in two-dimensional MXene for supercapacitor applications: progress, challenges, and perspectives. *Nanomaterials* **13**, 919 (2023).
- 47 Ponnalagar, D., Hang, D.-R., Liang, C.-T. & Chou, M. M. Recent advances and future prospects of low-dimensional Mo₂C MXene-based electrode for flexible electrochemical energy storage devices. *Progress in Materials Science* **145**, 101308 (2024).
- 48 Kumar, Y., Gupta, M. & Sharma, S. Study of pristine and functionalized V₂C and Mo₂C MXenes as novel electrode material for supercapacitors. *Journal of Molecular Graphics and Modelling* **118**, 108366 (2023).
- 49 Du, X. *et al.* Enhancing the electrochemical performance of d-Mo₂CT_x MXene in lithium-ion batteries and supercapacitors by sulfur decoration. *Ceramics International* **49**, 19737-19745 (2023).
- 50 Rajendran, K. *et al.* Synthesis, formation mechanism and supercapacitor performance of MoS₂/Mo₂C/C nanofibers. *Journal of Alloys and Compounds* **980**, 173549 (2024).
- 51 Çakır, D., Sevik, C., Gülseren, O. & Peeters, F. M. Mo₂C as a high capacity anode material: A first-principles study. *Journal of Materials Chemistry A* **4**, 6029-6035 (2016).
- 52 Halim, J. *et al.* Synthesis and characterization of 2D molybdenum carbide (MXene). *Advanced Functional Materials* **26**, 3118-3127 (2016).
- 53 Jin, S. *et al.* Carbon dioxide adsorption of two-dimensional Mo₂C MXene. *Diamond and Related Materials* **128**, 109277 (2022).
- 54 Kadam, S. A., Kadam, K. P. & Pradhan, N. R. Advancements in 2D MXene-based supercapacitor electrodes: synthesis, mechanisms, electronic structure engineering, flexible wearable energy storage for real-world applications, and future prospects. *Journal of Materials Chemistry A* **12**, 17992-18046 (2024).
- 55 Lukatskaya, M. R. *et al.* in *MXenes* 723-743 (Jenny Stanford Publishing, 2023).
- 56 Frackowiak, E. Carbon materials for supercapacitor application. *Physical chemistry chemical physics* **9**, 1774-1785 (2007).
- 57 Li, Y. *et al.* Molten salt derived Mo₂CT_x MXene with excellent catalytic performance for hydrogen evolution reaction. *Acta Physico-Chimica Sinica* **40**, 2306031 (2024).
- 58 Khanal, R. & Irle, S. Effect of surface functional groups on MXene conductivity. *The Journal of Chemical Physics* **158** (2023).
- 59 Anasori, B., Lukatskaya, M. R. & Gogotsi, Y. in *MXenes* 677-722 (Jenny Stanford Publishing, 2023).
- 60 Tang, M. *et al.* Surface terminations of MXene: synthesis, characterization, and properties. *Symmetry* **14**, 2232 (2022).
- 61 Palumbo, S. *et al.* Silicon few-layer graphene nanocomposite as high-capacity and high-rate anode in lithium-ion batteries. *ACS Applied Energy Materials* **2**, 1793-1802 (2019).

- 62 Greco, E. *et al.* Few-layer graphene improves silicon performance in Li-ion battery anodes. *Journal of Materials Chemistry A* **5**, 19306-19315 (2017).
- 63 Polverino, S. *et al.* Few-layers graphene-based cement mortars: production process and mechanical properties. *Sustainability* **14**, 784 (2022).
- 64 Bonaccorso, F. *et al.* Graphene, related two-dimensional crystals, and hybrid systems for energy conversion and storage. *Science* **347**, 1246501 (2015).
- 65 Mendhe, A. & Panda, H. A review on electrolytes for supercapacitor device. *Discover Materials* **3**, 29 (2023).
- 66 Banda, H. *et al.* High-capacitance pseudocapacitors from Li⁺ ion intercalation in nonporous, electrically conductive 2D coordination polymers. *Journal of the American Chemical Society* **143**, 2285-2292 (2021).
- 67 Jiang, Q. *et al.* A redox-active 2D metal–organic framework for efficient lithium storage with extraordinary high capacity. *Angewandte Chemie International Edition* **59**, 5273-5277 (2020).
- 68 Pal, B., Yang, S., Ramesh, S., Thangadurai, V. & Jose, R. Electrolyte selection for supercapacitive devices: a critical review. *Nanoscale advances* **1**, 3807-3835 (2019).
- 69 Li, X.-y., Wang, Q. & Wang, H.-w. Conversion of carbon nanotubes into curved graphene with improved capacitance. *New Carbon Materials* **36**, 835-842 (2021).
- 70 Arole, K. *et al.* Water-dispersible Ti₃C₂T_x MXene nanosheets by molten salt etching. *Iscience* **24** (2021).
- 71 Kruger, D. D., García, H. & Primo, A. Molten salt derived MXenes: synthesis and applications. *Advanced Science* **11**, 2307106 (2024).
- 72 Antony Jose, S., Price, J., Lopez, J., Perez-Perez, E. & Menezes, P. L. Advances in MXene Materials: Fabrication, Properties, and Applications. *Materials* **18**, 4894 (2025).
- 73 Huang, P. & Han, W.-Q. Recent advances and perspectives of lewis acidic etching route: an emerging preparation strategy for MXenes. *Nano-Micro Letters* **15**, 68 (2023).
- 74 Kumar, S. *et al.* Effect of Ti₃C₂T_x MXenes etched at elevated temperatures using concentrated acid on binder-free supercapacitors. *RSC advances* **10**, 41837-41845 (2020).
- 75 Zhang, X. *et al.* Synthesis of NiFe-MOF@ NiFeTe nanoparticle-rod heterostructure on nickel foam for high-performance hybrid supercapacitors. *Applied Surface Science* **616**, 156533 (2023).
- 76 Patel, A., Patel, S. K., Singh, R. & Patel, R. Review on recent advancements in the role of electrolytes and electrode materials on supercapacitor performances. *Discover Nano* **19**, 188 (2024).
- 77 Zhong, C. *et al.* A review of electrolyte materials and compositions for electrochemical supercapacitors. *Chemical Society Reviews* **44**, 7484-7539 (2015).
- 78 Bogdanowicz, R. *et al.* Enhanced charge storage mechanism and long-term cycling stability in diamondized titania nanocomposite supercapacitors operating in aqueous electrolytes. *The Journal of Physical Chemistry C* **124**, 15698-15712 (2020).
- 79 Chodankar, N. R. *et al.* True meaning of pseudocapacitors and their performance metrics: asymmetric versus hybrid supercapacitors. *Small* **16**, 2002806 (2020).
- 80 Wu, C.-L. & Chen, D.-H. Fabrication of rGO/CoS_x-rGO/rGO hybrid film via coassembly and sulfidation of 2D metal organic framework nanoflakes and graphene oxide as free-standing supercapacitor electrode. *Journal of Alloys and Compounds* **872**, 159702 (2021).
- 81 Li, Z.-X. *et al.* Novel porous carbon nanosheet derived from a 2D Cu-MOF: Ultrahigh porosity and excellent performances in the supercapacitor cell. *Carbon* **144**, 540-548 (2019).
- 82 Pal, B., Yang, S., Ramesh, S., Thangadurai, V. & Jose, R.

- 83 Chae, J. H. & Chen, G. Z. Influences of ions and temperature on performance of carbon nano-
particulates in supercapacitors with neutral aqueous electrolytes. *Particuology* **15**, 9-17 (2014).
- 84 Gao, H., Virya, A. & Lian, K. Monovalent silicotungstate salts as electrolytes for electrochemical
supercapacitors. *Electrochimica Acta* **138**, 240-246 (2014).
- 85 Halankar, K. K. *et al.* Experimental and theoretical study on rGO-decorated Mo₂C composite as
the anode material for lithium ion batteries. *Energy & Fuels* **35**, 12556-12568 (2021).
- 86 Wang, B., Wang, G. & Wang, H. Hybrids of Mo₂C nanoparticles anchored on graphene sheets as
anode materials for high performance lithium-ion batteries. *Journal of Materials Chemistry A* **3**,
17403-17411 (2015).
- 87 Li, H. *et al.* Freestanding MoO₂/Mo₂C imbedded carbon fibers for Li-ion batteries. *Physical
Chemistry Chemical Physics* **19**, 2908-2914 (2017).
- 88 Ragupathi, J. & Annal Therese, H. Synthesis of One-Dimensional Mo₂C-Embedded Carbon
Nanofibers with Enhanced Lithium Storage Capacity for Lithium-Ion Batteries. *ChemistrySelect* **7**,
e202201924 (2022).
- 89 Ou, X. *et al.* In situ X-ray diffraction investigation of CoSe₂ anode for Na-ion storage: Effect of cut-
off voltage on cycling stability. *Electrochimica Acta* **258**, 1387-1396 (2017).
- 90 Lu, Y.-C., Mansour, A. N., Yabuuchi, N. & Shao-Horn, Y. Probing the origin of enhanced stability of
“AlPO₄” nanoparticle coated LiCoO₂ during cycling to high voltages: combined XRD and XPS
studies. *Chemistry of Materials* **21**, 4408-4424 (2009).
- 91 Huang, Y., Jin, F.-M., Chen, F.-J. & Chen, L. Improved cycle stability and high-rate capability of
Li₃VO₄-coated Li [Ni_{0.5}Co_{0.2}Mn_{0.3}] O₂ cathode material under different voltages. *Journal of
Power Sources* **256**, 1-7 (2014).
- 92 Zhou, J. *et al.* Ultrahigh volumetric capacitance and cyclic stability of fluorine and nitrogen co-
doped carbon microspheres. *Nature communications* **6**, 8503 (2015).
- 93 Leng, K. *et al.* Phase restructuring in transition metal dichalcogenides for highly stable energy
storage. *Acs Nano* **10**, 9208-9215 (2016).
- 94 Bellani, S. *et al.* Scalable production of graphene inks via wet-jet milling exfoliation for screen-
printed micro-supercapacitors. *Advanced Functional Materials* **29**, 1807659 (2019).
- 95 Hu, R. Y. *et al.* Preparation and electrochemical properties of bimetallic carbide
Fe₃Mo₃C/Mo₂C@ carbon nanotubes as negative electrode material for supercapacitor. *Journal
of Energy Storage* **72**, 108656 (2023).
- 96 Upadhyay, S. & Pandey, O. One-pot synthesis of pure phase molybdenum carbide (Mo₂C and
MoC) nanoparticles for hydrogen evolution reaction. *International journal of hydrogen energy*
45, 27114-27128 (2020).
- 97 Anwar, S. *et al.* Synthesis and electrochemical performance of 2D molybdenum carbide (MXene)
for supercapacitor applications. *Electrochimica Acta* **512**, 145508 (2025).
- 98 Chusuei, C. C. & Nepal, R. C. Role of defects and exposed graphene in carbon nanomaterial-based
electrocatalysts. *New Journal of Chemistry* **48**, 260-267 (2024).
- 99 Liu, H. *et al.* Defect engineering of 2D materials for electrochemical energy storage. *Advanced
Materials Interfaces* **7**, 2000494 (2020).
- 100 Simon, P. & Gogotsi, Y. Capacitive energy storage in nanostructured carbon–electrolyte systems.
Accounts of chemical research **46**, 1094-1103 (2013).
- 101 Lei, C. *et al.* Charge engineering of Mo₂C@ defect-rich N-doped carbon nanosheets for efficient
electrocatalytic H₂ evolution. *Nano-Micro Letters* **11**, 45 (2019).

- 102 Sylla, N. F. *et al.* Enhanced electrochemical behavior of peanut-shell activated carbon/molybdenum oxide/molybdenum carbide ternary composites. *Nanomaterials* **11**, 1056 (2021).
- 103 Zhu, J. *et al.* The effect of various electrolyte cations on electrochemical performance of polypyrrole/RGO based supercapacitors. *Physical Chemistry Chemical Physics* **17**, 28666-28673 (2015).
- 104 Bard, A. J., Faulkner, L. R. & White, H. S. *Electrochemical methods: fundamentals and applications*. (John Wiley & Sons, 2022).
- 105 Bagheri, A. *et al.* Coexistence of Redox-Active Metal and Ligand Sites in Copper-Based Two-Dimensional Conjugated Metal–Organic Frameworks as Active Materials for Battery-Supercapacitor Hybrid Systems. *ChemSusChem* **18**, e202401454 (2025).
- 106 Shao, Y. *et al.* Design and mechanisms of asymmetric supercapacitors. *Chemical reviews* **118**, 9233-9280 (2018).
- 107 Vignesh, G. *et al.* Nitrogen doped reduced graphene oxide/ZnCo₂O₄ nanocomposite electrode for hybrid supercapacitor application. *Materials Science and Engineering: B* **290**, 116328 (2023).
- 108 Qu, D., Ji, W. & Qu, H. Probing process kinetics in batteries with electrochemical impedance spectroscopy. *Communications Materials* **3**, 61 (2022).
- 109 Lazanas, A. C. & Prodromidis, M. I. Electrochemical impedance spectroscopy– a tutorial. *ACS measurement science au* **3**, 162-193 (2023).
- 110 Hadji, F., Omari, M., Mebarki, M., Gabouze, N. & Layadi, A. Zinc doping effect on the structural and electrochemical properties of LaCoO₃ perovskite as a material for hybrid supercapacitor electrodes. *Journal of Alloys and Compounds* **942**, 169047 (2023).
- 111 Qin, K., Baucom, J., Diao, L., Lu, Y. & Zhao, N. Compacted N-Doped 3D Bicontinuous Nanoporous Graphene/Carbon Nanotubes@ Ni-Doped MnO₂ Electrode for Ultrahigh Volumetric Performance All-Solid-State Supercapacitors at Wide Temperature Range. *Small* **18**, 2203166 (2022).
- 112 Zhao, X. *et al.* Hierarchical nanocages assembled by NiCo-layered double hydroxide nanosheets for a high-performance hybrid supercapacitor. *ACS Applied Materials & Interfaces* **14**, 34781-34792 (2022).
- 113 Portet, C., Taberna, P., Simon, P. & Laberty-Robert, C. Modification of Al current collector surface by sol–gel deposit for carbon–carbon supercapacitor applications. *Electrochimica Acta* **49**, 905-912 (2004).
- 114 Yadav, S. & Kurra, N. Diffusion kinetics of ionic charge carriers across Ti₃C₂T_x MXene-aqueous electrochemical interfaces. *Energy Storage Materials* **65**, 103094 (2024).
- 115 Ho, C., Raistrick, I. & Huggins, R. Application of A-C techniques to the study of lithium diffusion in tungsten trioxide thin films. *Journal of The Electrochemical Society* **127**, 343-350 (1980).
- 116 Lukatskaya, M. R. *et al.* Cation intercalation and high volumetric capacitance of two-dimensional titanium carbide. *Science* **341**, 1502-1505 (2013).
- 117 Zhang, C. *et al.* Transparent, flexible, and conductive 2D titanium carbide (MXene) films with high volumetric capacitance. *Advanced materials* **29**, 1702678 (2017).
- 118 Beknalkar, S. *et al.* Fabrication of high energy density supercapacitor device based on hollow iridium oxide nanofibers by single nozzle electrospinning. *Applied Surface Science* **546**, 149102 (2021).
- 119 Zhang, T. *et al.* Delamination of chlorine-terminated MXene produced using molten salt etching. *Chemistry of materials* **36**, 1998-2006 (2024).

- 120 Castillo, A. D. R. *et al.* High-yield production of 2D crystals by wet-jet milling. *Materials Horizons* **5**, 890-904 (2018).
- 121 Beydaghi, H. *et al.* 3D printed silicon-few layer graphene anode for advanced Li-ion batteries. *RSC advances* **11**, 35051-35060 (2021).
- 122 Levchenko, S. *et al.* Influence of Ion Diffusion on the Lithium–Oxygen Electrochemical Process and Battery Application Using Carbon Nanotubes–Graphene Substrate. *ACS Applied Materials & Interfaces* **15**, 39218-39233 (2023).
- 123 Zappia, M. I. *et al.* Graphene vs. carbon black supports for Pt nanoparticles: Towards next-generation cathodes for advanced alkaline electrolyzers. *Electrochimica Acta* **462**, 142696 (2023).
- 124 Eredia, M. *et al.* High-energy density aqueous supercapacitors: The role of electrolyte pH and KI redox additive. *APL Materials* **10** (2022).
- 125 Bagheri, A. *et al.* Functionalized metallic 2D transition metal dichalcogenide-based solid-state electrolyte for flexible all-solid-state supercapacitors. *Acs Nano* **16**, 16426-16442 (2022).
- 126 Gogotsi, Y. & Simon, P. True performance metrics in electrochemical energy storage. *science* **334**, 917-918 (2011).
- 127 Kong, J. *et al.* High-mass-loading porous Ti₃C₂T_x films for ultrahigh-rate pseudocapacitors. *ACS Energy Letters* **5**, 2266-2274 (2020).
- 128 Wang, J. *et al.* In situ oxidized Mo₂CT_x MXene film via electrochemical activation for smart electrochromic supercapacitors. *Journal of Colloid and Interface Science* **684**, 170-179 (2025).
- 129 Kirubasankar, B. *et al.* Construction of heterogeneous 2D layered MoS₂/MXene nanohybrid anode material via interstratification process and its synergetic effect for asymmetric supercapacitors. *Applied Surface Science* **534**, 147644 (2020).
- 130 Nian, Q. *et al.* Designing electrolyte structure to suppress hydrogen evolution reaction in aqueous batteries. *ACS Energy Letters* **6**, 2174-2180 (2021).
- 131 Ahn, H., Kim, D., Lee, M. & Nam, K. W. Challenges and possibilities for aqueous battery systems. *Communications Materials* **4**, 37 (2023).

Figures

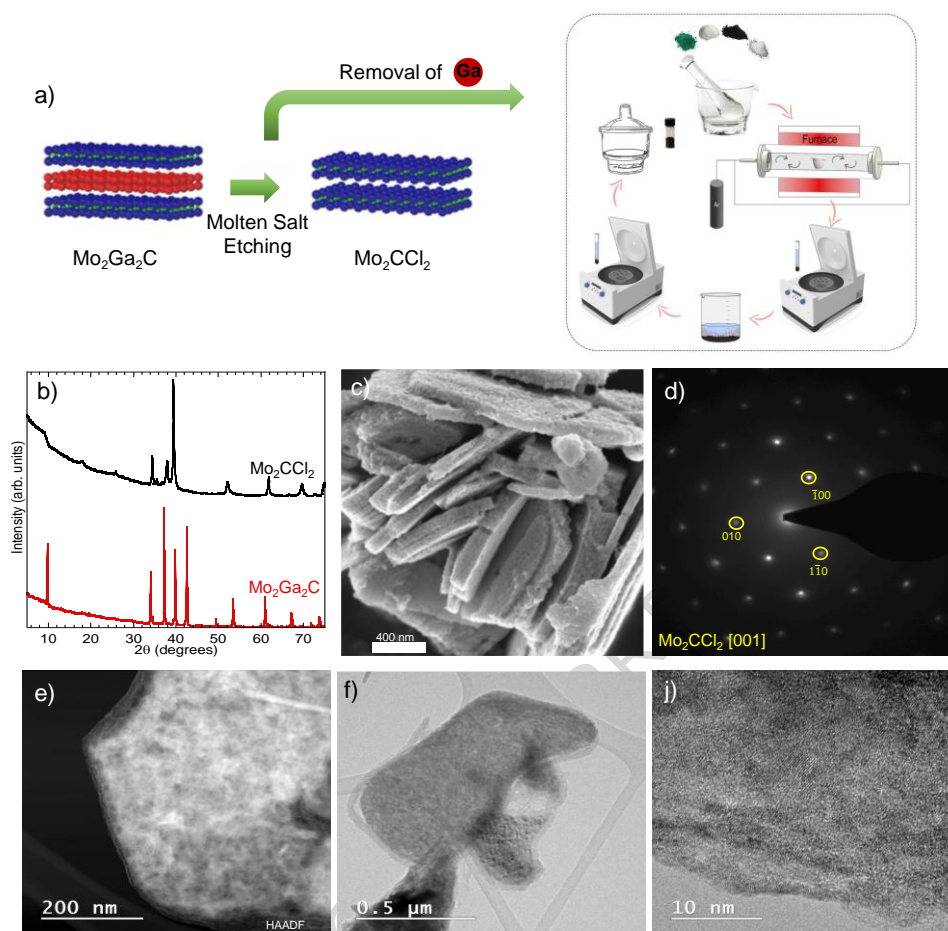


Figure 1. Synthesis protocol and structural characterization of Mo_2CCl_2 . a) schematic illustration of the synthesized Mo_2CCl_2 . b) XRD patterns of Mo_2CCl_2 and parent $\text{Mo}_2\text{Ga}_2\text{C}$. c) SEM image of Mo_2CCl_2 particles. d) SAED along the [001] axis. e) HAADF STEM image of Mo_2CCl_2 particle. f) and j) are TEM images at low and high magnification.

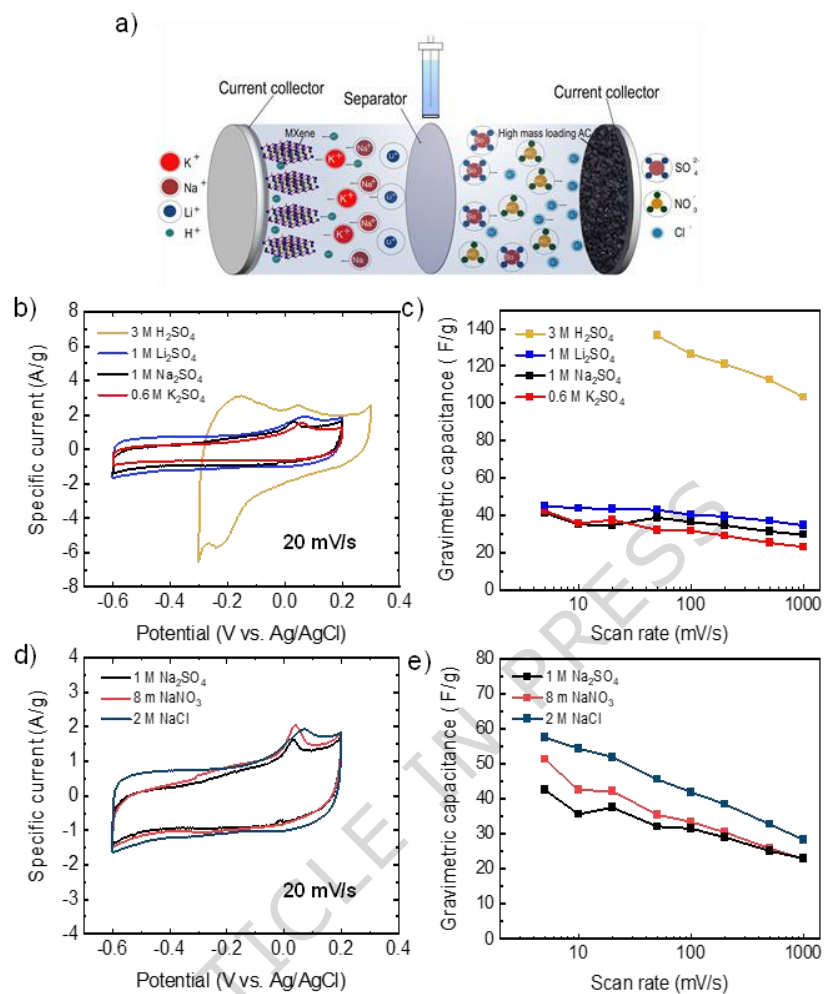


Figure 2. Three-electrode electrochemical characterization of the $\text{Mo}_2\text{CCl}_2/\text{FLG}$ electrode in different electrolytes. a) Schematic of the three-electrode configuration used for the $\text{Mo}_2\text{CCl}_2/\text{FLG}$ electrode b, d) CV curves measured for $\text{Mo}_2\text{CCl}_2/\text{FLG}$ electrodes in different electrolytes at a potential scan rate of 20 mV/s. c, e) C_g of the electrodes as a function of the potential scan rate.

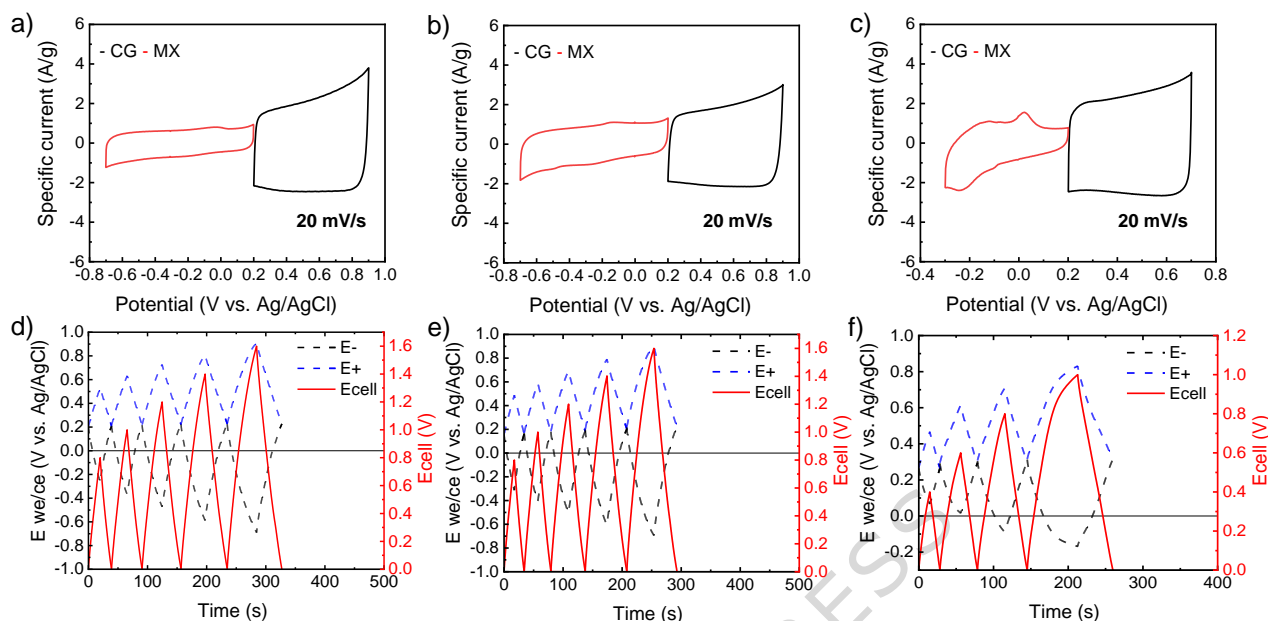


Figure 3. The electrochemical stability of $\text{Mo}_2\text{CCl}_2/\text{FLG}$ electrodes. CV curves of a) $\text{Mo}_2\text{CCl}_2/\text{FLG} // \text{CG}/\text{FLG}-8 \text{ m NaNO}_3$, b) $\text{Mo}_2\text{CCl}_2/\text{FLG} // \text{CG}/\text{FLG}-2 \text{ M NaCl}$ and c) $\text{Mo}_2\text{CCl}_2/\text{FLG} // \text{CG}/\text{FLG}-3 \text{ M H}_2\text{SO}_4$, measured at 20 mV/s in a three-electrode cell configuration. GCD curves with real-time electrode potentials and cell voltage of ASCs d) $\text{Mo}_2\text{CCl}_2/\text{FLG} // \text{CG}/\text{FLG}-8 \text{ m NaNO}_3$, e) $\text{Mo}_2\text{CCl}_2/\text{FLG} // \text{CG}/\text{FLG}-2 \text{ M NaCl}$ and f) $\text{Mo}_2\text{CCl}_2/\text{FLG} // \text{CG}/\text{FLG}-3 \text{ M H}_2\text{SO}_4$.

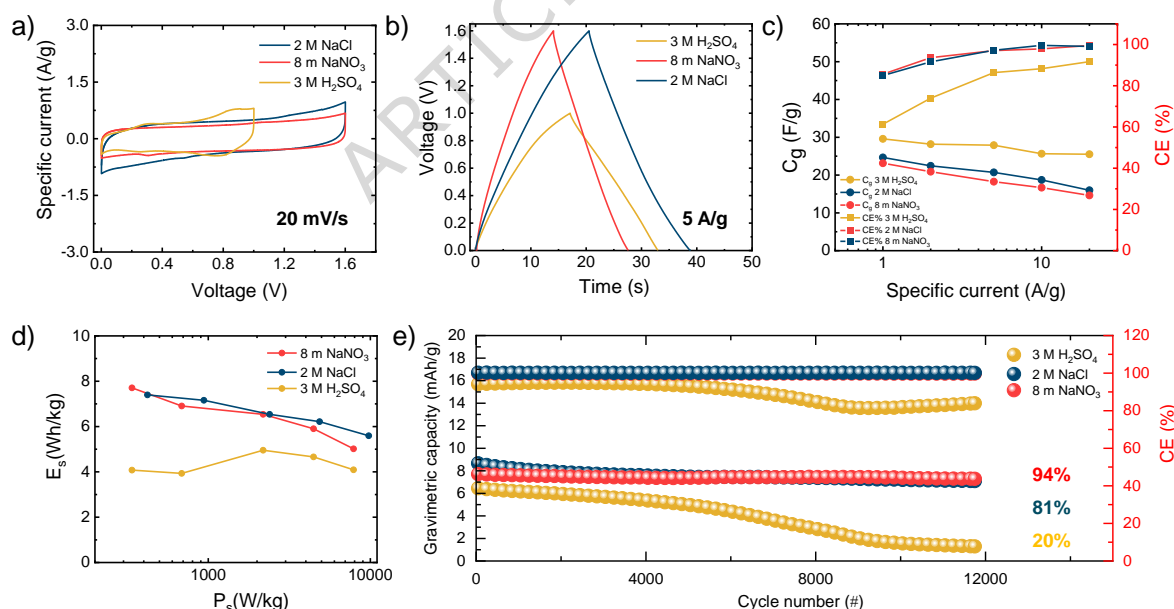


Figure 4. Electrochemical characterization of the investigated $\text{Mo}_2\text{CCl}_2/\text{FLG} // \text{CG}/\text{FLG}$ ASCs. a) CV curves of the ASC recorded in 8 m NaNO_3 (red curves), 2 M NaCl (dark cyan curves), and $3 \text{ M H}_2\text{SO}_4$ (orange curves). b) GCD profiles of the SCs recorded in 8 m NaNO_3 , 2 M NaCl , and $3 \text{ M H}_2\text{SO}_4$. c) C_g and d) CE of the investigated ASCs as a function of the specific current (data extrapolated from the GCD profiles), e) Ragone plots and f) C_g retention of the investigated ASCs over 12000 GCD cycles at 5 A/g .

Additional information

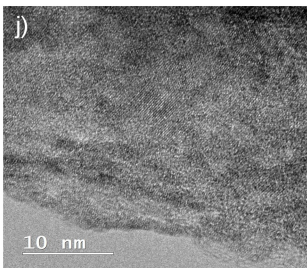
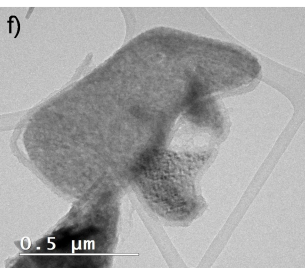
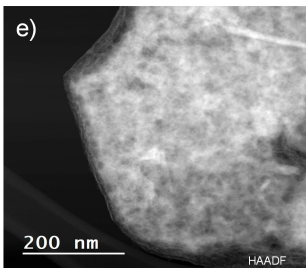
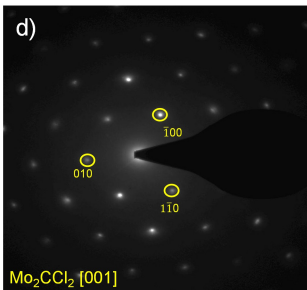
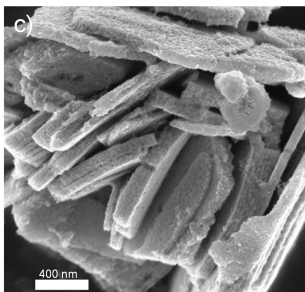
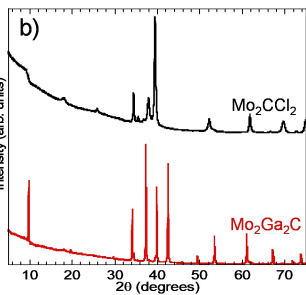
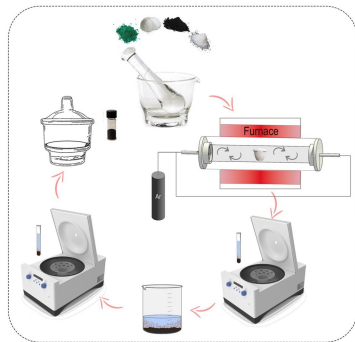
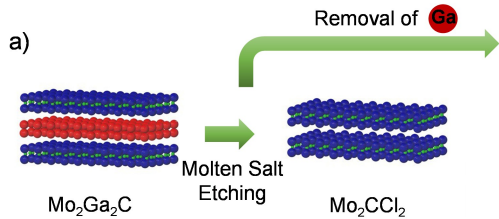
Supplementary information The online version contains supplementary material available at

Correspondence and requests for materials should be addressed to Francesco Bonaccorso. f.bonaccorso@bedimensional.it

Reprints and permissions information is available at <http://www.nature.com/reprints>.

Publisher's note Springer Nature remains neutral with regard to jurisdictional claims in published maps and institutional affiliations.

Open Access This article is licensed under a Creative Commons Attribution 4.0 International License, which permits use, sharing, adaptation, distribution and reproduction in any medium or format, as long as you give appropriate credit to the original author(s) and the source, provide a link to the Creative Commons licence, and indicate if changes were made. The images or other third party material in this article are included in the article's Creative Commons licence, unless indicated otherwise in a credit line to the material. If material is not included in the article's Creative Commons licence and your intended use is not permitted by statutory regulation or exceeds the permitted use, you will need to obtain permission directly from the copyright holder. To view a copy of this licence, visit <http://creativecommons.org/licenses/by/4.0/>.



a)

